

## RESEARCH ARTICLE

Polymer  
COMPOSITES

WILEY

# Comparison of damage mechanisms in chopped strand mat and woven roving mat composites under cyclic tension

Mritunjay M. Hiremath<sup>1</sup> | Timo Bernthaler<sup>2</sup> | Pascal Anger<sup>3</sup> |  
Sushil K. Mishra<sup>1</sup> | Anirban Guha<sup>1</sup> | Asim Tewari<sup>1</sup>

<sup>1</sup>Department of Mechanical Engineering,  
Indian Institute of Technology Bombay,  
Mumbai, India

<sup>2</sup>Materials Research Institute, Aalen  
University, Aalen, Germany

<sup>3</sup>Industrial Quality and Research, Carl  
Zeiss Microscopy GmbH, Oberkochen,  
Germany

## Correspondence

Asim Tewari, Department of Mechanical  
Engineering, Indian Institute of  
Technology Bombay, Mumbai 400076,  
India.  
Email: [asim.tewari@iitb.ac.in](mailto:asim.tewari@iitb.ac.in)

## Funding information

Indo-German Science and Technology  
Centre, Grant/Award Number: IGSTC/IF  
Call 2022/PIEF - (MH)/23/2022-23/

## Abstract

Glass fiber reinforced polymer (GFRP) composites with chopped strand mat (CSM) and woven roving mat (WRM) reinforcements are widely used in high-pressure piping due to their favorable strength-to-weight ratio. However, cyclic loading from vibrations and pulsating forces can induce internal microstructural damage, ultimately leading to performance degradation. A thorough understanding of this damage mechanism is imperative for its mitigation, necessitating a detailed examination. The present study aims to investigate the fatigue response and damage mechanisms in CSM and WRM composites subjected to tension-tension cyclic loading. Scanning electron microscopy analysis of edge sections revealed the development of perpendicular microcracks in both composites. CSM composites exhibited fatigue cracks parallel to the loading direction and higher levels of parallel interface debonding compared to perpendicular matrix cracks. Finite element analysis of the representative volume element revealed the role of shear stress in the matrix in initiating parallel cracks, thereby explaining the damage initiation mechanism in CSM. These findings highlight the distinct damage mechanisms arising from the differing fiber arrangements in CSM and WRM composites, providing valuable insights for optimizing their performance under cyclic loading conditions.

## Highlights

- Fatigue response of CSM and WRM was influenced by fiber orientation and weaving pattern.
- Perpendicular fibers were the most probable fibers to have their interface form a crack.
- Fatigue cracks parallel to the direction of loading were observed in CSM composites.
- Quantified the true 3D internal microstructural damages for the first time.

## KEYWORDS

damage mechanics, electron microscopy, fatigue, glass fibers

## 1 | INTRODUCTION

Glass fiber-reinforced polymer (GFRP) composites have gained significant popularity worldwide as potential candidates for replacing conventional materials in structural applications. In addition to their high strength and stiffness-to-weight ratios, these composites possess unique anisotropic properties, making them excellent choices for high-pressure pipes.<sup>1,2</sup> However, most engineered structural components made from these materials are subject to cyclic loading, including vibrations and pulsating forces, which can cause irreversible internal microstructural damage. This damage leads to a cumulative degradation of the material's properties. Therefore, to properly integrate these damage mechanisms into the multiscale model, the first step is to conduct extensive damage investigations.

This paper investigates the tension-tension fatigue damage mechanisms in chopped strand mat (CSM) and woven roving mat (WRM) composites. In commercial practice, WRM, which has greater stiffness and strength, is often combined with CSM in high-stress areas, particularly in pipes and pressure vessel applications. Over the last four decades, extensive analytical and experimental research has been carried out to understand the fatigue damage mechanisms of these GFRPs.<sup>3,4</sup> Despite this, most research in this area focuses on developing predictive models based on the S-N curve and a phenomenological approach.<sup>5-9</sup> While these methods have provided valuable insights into the macroscopic behavior of materials, they fall short of explaining the underlying microstructural damage mechanisms due to the complex nature of damage development under cyclic loading.

The damage mechanism in woven fabrics is very well-documented across several studies in the literature. Under tension-tension cyclic loading, WRM composites exhibit a progressive damage process.<sup>10-12</sup> Initially, damage begins at the interfacial bond between the resin and glass due to stress concentration, followed by the formation of cracks perpendicular to the loading direction in the off-axis bundles. As the number of cycles increases, meta-delamination is observed to initiate and propagate. Lamon et al.,<sup>13</sup> analyzed the influence of the weaving patterns (plain and twill) on damage progression under cyclic tensile loads. They reported that plain weave layers exhibited a faster crack density evolution compared to the twill weave layers, despite being subjected to the same stress levels. Additionally, bundle features such as areal weight, fiber content, cross-sectional shape, and waviness influence damage evolution by affecting local stress distribution.<sup>14</sup> Daggumati et al.<sup>15</sup> conducted an experimental fatigue damage analysis on 5-harness satin weave composites under tension-tension

fatigue, revealing that microscopic observations showed a significantly higher straightening of the load-carrying warp yarns in tension-tension fatigue tests compared to static tests. This phenomenon was attributed to the extensive relative sliding between the fiber bundles caused by meta-delaminations formed during the fatigue load. Xu et al.<sup>16</sup> investigated the tension-tension fatigue characteristics of two types of twill weave carbon/epoxy composite materials, concluding that the higher crimp in twill composites results in greater stress concentration, thereby reducing fatigue life. Contrary to unidirectional composites, the weave pattern influences the stress/strain distribution, thus affecting the evolution of fatigue damage.<sup>17-20</sup>

Useful information regarding fatigue crack development in CSM composites is provided in Refs. [21,22]. A recent study by Sun et al.<sup>23</sup> reveals the static and fatigue behavior of chopped glass fiber-reinforced sheet molding composites. They reported that cracks tend to initiate within the fiber bundles, transversely oriented to the loading direction. Belmonte et al.<sup>24</sup> conducted a damage investigation on short glass fiber-reinforced polyamide composites under fatigue loading. Their study concluded with new findings that describe a damage initiation scenario, taking into account the local fiber orientation and the mechanisms responsible for the first event of damage in the material. Owen and Dukes<sup>25</sup> have reported that failure in GFRP composite is strongly influenced by the presence of fibers lying perpendicular to the direction of loading, while the reinforcement is due to the strengthening effect of fibers aligned in the direction of loading. Moreover, the authors suggest that failure certainly appears for GFRP formulations containing multi-directional continuous reinforcements or randomly placed short reinforcements, where damage originates at the fibers perpendicular to the loading direction. However, it remains uncertain whether the failure is consistently driven by the tensile load.

Though not directly critical to the ultimate fatigue failure, the presence of any form of microstructural damage poses a latent danger that cannot be underestimated. Numerous works in the literature demonstrate, at least qualitatively, that all forms of microstructural damage increase throughout the fatigue life.<sup>13,26-28</sup> In this context, damage characterization involves both qualitative damage detection and damage quantification. Damage quantification requires a methodology for direct damage observation which is possible through X-ray tomography and microscopy-based destructive techniques. However, X-ray tomography is limited by spatial resolution. The extent to which damage mechanisms are observed in detail depends on both the observation method and the sensitivity of the equipment

used. Hence, scanning electron microscopy (SEM) needs to be employed for surface-based quantification, such as matrix cracking and interface debonding, in combination with the stereology technique.<sup>29–32</sup> This approach provides robust and unbiased true 3D internal microstructural damage data from observations on 2D sections.

The focus is on analyzing the fiber-matrix interface after subjecting the two composites to tension-tension cyclic loading. It is important to recall that, in composite materials, the initiation and propagation mechanism of fatigue damage depends on the stress experienced by each constituent element. Even if the composite material is subjected to the same uniaxial loads, the stress state within the composite material differs. This variation is due to the spatial arrangement of the fibers and the differences in fiber volume fractions. Hence, it becomes crucial to analyze the damage development in CSM and WRM composites under tension-tension cyclic loading.

Accordingly, in this paper, the damage analysis was carried out separately for CSM and WRM composites at the micro-length scale. Specifically, this research work focuses on understanding the damage mechanisms exhibited by CSM and obtaining a comparison of the damage mechanisms occurring between the two composites. By discerning the intricate interplay between microstructure and tension-tension fatigue behavior, this research aims to elucidate on how and why damage mechanisms differ within the broader GFRP composite realm. This investigation at that micro-length scale has led to some key novel observations, which, to the author's best knowledge, have never been reported in the recent open literature. Eventually, true 3D internal microstructural damage, such as parallel and perpendicular interface debonding surface area per unit volume, was directly quantified with observations on 2D sections, irrespective of the load history of the structure. A model to explain the crack initiation mechanism in CSM was also developed. The key features of the model were validated using numerical analysis and quantitative microscopy.

## 2 | MATERIALS AND TESTING PROCEDURE

### 2.1 | Composite materials and specimen preparation

The glass fiber-reinforced polymer laminates were procured from Sunrise Industries (India) Ltd., Gujarat, India. The procured large panels (500 mm × 500 mm) comprised of plain weave E-glass fabric in woven roving mat (WRM) form and E-glass fabric in CSM form. The respective mats were stacked with vinyl ester resin (Derakane Momentum 411–350). In order to determine the volume fraction of fiber, the resin burn-off method was followed as per ASTM standard D3171. The nominal weight (grams per square meter (GSM)), number of layers, and the nominal volume fraction of respective composites are listed in Table 1.

All the test specimens for monotonic and fatigue tests were water jet cut out of the composite panels. The tensile and fatigue coupon specimens were prepared according to the geometry as shown in Figure 1. The specimen

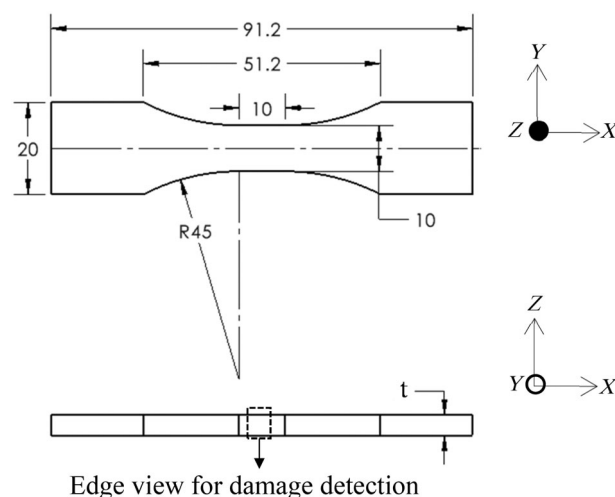


**FIGURE 1** Specimen geometry used for tensile and fatigue tests from top view and edge view (dimensions in mm).

**TABLE 1** Composites made by hand layup of E-glass and epoxy vinyl ester resin (Derakane Momentum 411-350) with various GSM values used for this research and respective details of the monotonic and cyclic tests conducted.

Material	Nominal weight (GSM)	Number of layers	Glass volume fraction by Burn off test ( $V_v$ )	Monotonic tensile testing	SN curve for fatigue testing (at $R = 0.5$ )	Interrupted fatigue testing
WRM	610	8	0.387	y	–	–
WRM	800	5	0.387	y	–	–
WRM	1000	5	0.400	y	y	y
CSM	300	8	0.194	y	–	–
CSM	450	6	0.201	y	y	y

geometry used for these two tests was completely based on a similar design used in a Ref. [33].

## 2.2 | Monotonic tensile and fatigue testing

The monotonic quasi-static tensile and fatigue tests were performed on a 100 kN closed-loop servo-hydraulic axial fatigue MTS-Landmark system at an ambient temperature ( $\sim 25.6^\circ\text{C}$ ) until fracture. The uniaxial tension tests for WRM and CSM composites were performed in accordance with ISO 527-4 test conditions, with a displacement rate of 1 mm/min. A minimum of three tests were performed for each material to evaluate their properties. The tensile elastic modulus was obtained using the strain data acquired from an MTS make 10 mm extensometer. Using a spring mechanism, the extensometer was attached directly to the coupon specimens ensuring that the strain values acquired were solely a result of the coupon specimen's deformation. The constant amplitude uniaxial tension-tension fatigue tests were performed under load control conditions until fracture, with a minimum to maximum stress ratio ( $R$ -ratio) of 0.5. This stress ratio was chosen based on established literature within the field, particularly in relation to CSM-WRM GFRP pipes used in power station cooling water systems. These pipes are subjected to a complex loading pattern, which includes a background static load superimposed with sinusoidal variations.<sup>2,21</sup> Further, the objective of the fatigue test was to determine the load factor (the ratio of maximum stress to ultimate tensile strength) for the subsequent phase of damage characterization experiments. The load factor was chosen (based on the SN curve) to ensure that the composite could endure 100,000 fatigue cycles. For WRM (1000 gsm) and CSM (450 gsm) composites, load factors were selected relative to their maximum tensile strength. The load factor ( $L_R$ ) utilized for interrupted fatigue experiments for both WRM (1000 gsm) and CSM (450 gsm) composite was 0.58. All tests were conducted in a room-temperature environment and at a frequency of 10 Hz. The cyclic loading was conducted with respect to the fatigue standards of ISO 13003.<sup>34</sup> A total of nine specimens were tested to generate the SN curve, with a minimum of one repetition for each testing condition.

With the mentioned load factor of 0.58, another set of specimens was cyclically loaded (without leading to failure) to induce varying degrees of damage. This process was executed on several different specimens, each representing a different stage of fatigue damage. All these specimens were cyclically loaded for  $10^3$ ,  $10^4$  and  $10^5$  cycles and were subjected to sectional microscopic

analysis to assess the damage mechanisms. They were not subjected to further cyclic loads thereafter. Hence, this resulted in conducting a large number of tests for each type of material leading to a collection of different states of damage in the specimens. Throughout the fatigue loading process, the dynamic stiffness of all specimens was continuously tracked by recording the peak and valley loads and strains measured by the testing apparatus during each cycle. Based on this data, the axial modulus was calculated using the secant slope of the hysteresis loop.

## 2.3 | Microstructural damage characterization

For any microstructural-based characterization, preparing a sample properly for imaging is crucial. Surface-based damage in each specimen, subjected to a prescribed number of fatigue cycles, was characterized using scanning electron microscopy (SEM).

The sample preparation was undertaken at the Materials Research Institute, Aalen University, Germany, and the SEM imaging was conducted at Carl Zeiss Microscopy GmbH, Oberkochen, Germany. The preparation involved slicing, mounting, and polishing. Initially, the fatigued specimens were sliced into two parts, representing edge and front views, using the Secotom-10 (Struers Inc.) precision cutoff machine equipped with a diamond wheel. Slices were made at a feed rate of 0.02 mm/s and a speed of 3000 RPM, with extreme caution to avoid introducing any damage.

After slicing, the cold mounting procedure was followed, where these parts were embedded in epoxy molds and left to cure at room temperature for 24 h. To achieve the necessary surface finish, the molds underwent rough grinding and fine polishing using an automatic polisher (Tegramin-30 system by Struers Inc.). Between polishing steps, the polished samples were examined with a Zeiss Axioscope 7 upright optical motorized microscope to overview the damage distribution on the specific sectioned plane.

Before SEM imaging, the polished sections of WRM (1000 gsm) and CSM (450 gsm) were sputter-coated with gold using an automatic sputter machine. Then, a Zeiss Gemini SEM 560 was employed to examine the damages on a specific sectional plane, with SmartSEM interface software facilitating interaction with the SEM imaging process. The scanning speed was set to 4 (Dwell time of 0.8  $\mu\text{s}$ ) and the aperture to 60  $\mu\text{m}$ . The field of view was maintained at 350  $\mu\text{m} \times 350 \mu\text{m}$ , with a pixel size of 90 nm. The edge view was chosen as the observation plane to allow quantification of the fiber orientation



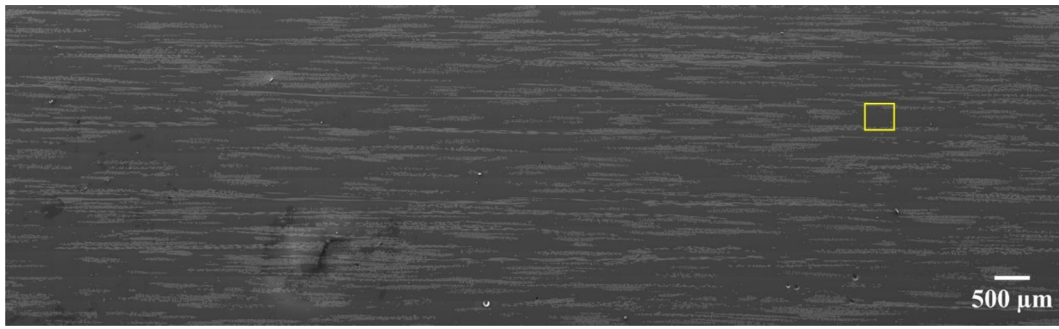


**FIGURE 2** A large area montage ( $39 \times 15$ ) of secondary electron detected SEM micrograph showing the entire edge section of CSM composite after 10,000 cycles.

distribution in the CSM composite's microstructures. Imaging utilized both secondary electron and in-lens detectors. To perform quantitative microscopy, a high-resolution, large-area montage of images was created by tiling contiguous micrographs<sup>35</sup> as shown in Figure 2. The  $39 \times 15$  montage, covering the entire edge view, was obtained for each composite. These images facilitated the quantitative analysis of fiber orientation distribution and surface-based, true 3D microstructural damage.

## 2.4 | Quantitative stereology for damage measurement

The microstructural damage is a three-dimensional physical constituent at the micrometer length scale. Through the application of the stereology technique,<sup>26,29–31</sup> these three-dimensional parameters that define the structure can be deduced from two-dimensional measurements obtained from micrograph images. The fundamental formulae of stereology were used to quantify the damage.

The parallel fiber/matrix debonding area is estimated from a micrograph having an interface debonding parallel to the loading direction. It is defined as shown in Equation (1),

$$((S_v)_{db})_{\parallel} = 2(P_L) \quad (1)$$

where  $((S_v)_{db})_{\parallel}$  is the parallel interface debonding surface area per unit volume in  $\mu\text{m}^{-1}$ .  $P_L$  is the average number of intersection points per unit length of a test line in  $\mu\text{m}^{-1}$ . The number of intersection points is calculated by superimposing an array of grid lines on a micrograph and counting the number of intersections of debonding and lines.

Similarly, the perpendicular fiber/matrix debonding area is estimated from a micrograph having interface debonding perpendicular to the loading direction. It is defined as shown in Equation (2),

$$((S_v)_{db})_{\perp} = 2(P_L) \quad (2)$$

where  $((S_v)_{db})_{\perp}$  is the perpendicular interface debonding surface area per unit volume in  $\mu\text{m}^{-1}$ .

The perpendicular matrix microstructural damage is a measure of crack surface density, which is defined as matrix crack surface area per unit volume. It is defined as shown in Equation (3),

$$((S_v)_m)_{\perp} = 2(P_L) \quad (3)$$

where  $((S_v)_m)_{\perp}$  is the perpendicular matrix crack surface area per unit volume in  $\mu\text{m}^{-1}$ . Perpendicular matrix cracks include both, perpendicular debonds that kink into the matrix and perpendicular cracks that propagate without encountering any fibers, as illustrated in Figure 3C.

A schematic picture of the meaning of parallel debonding, perpendicular debonding, and perpendicular matrix damage can be found in Figure 3.

## 2.5 | Finite element analysis

The detailed linear elastic finite element (FE) analysis under tension loading was conducted using the commercial finite element code ABAQUS<sup>®</sup> 6.13. This analysis aimed to understand the stress distribution resulting from the spatial arrangement of clustered fibers in CSM composite. For the simulation, a 3D numerical domain was considered, and the FE model for the CSM composite was simulated using an image-based Representative Volume Element (RVE). The RVE of the composite comprises six glass fibers embedded in a polymer matrix. The specifics of the RVE and the meshing elements employed are discussed in the numerical analysis section. In the FE model, a well-defined interface region is not delineated, as the primary goal was to ascertain the stress state

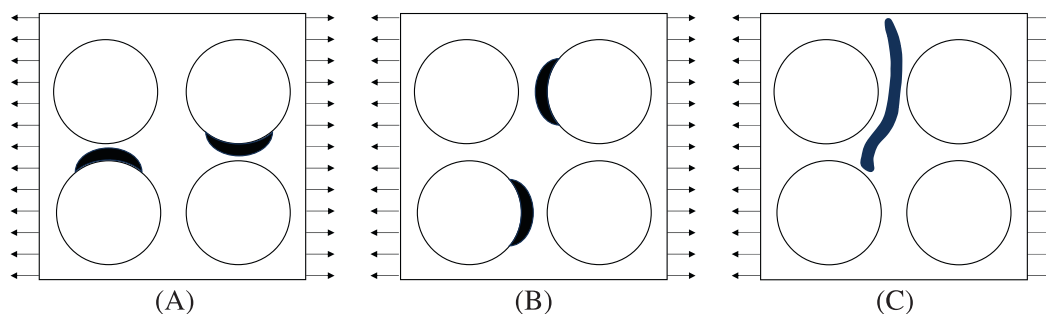


FIGURE 3 Drawing of (A) parallel debonding, (B) perpendicular debonding, and (C) perpendicular matrix damage in tension.

TABLE 2 Material properties of the constituents used for FE analysis.<sup>36</sup>

Material Properties	E-Glass	Vinyl ester
Longitudinal modulus, $E_L$ (GPa)	73	3.2
Transverse modulus, $E_T$ (GPa)	73	3.2
Poisson's ratio, $\nu$	0.2	0.4

within the matrix. Additionally, the interface between the glass fiber and the matrix was assumed to be perfectly bonded, disregarding any interfacial properties. Both the glass fiber and the matrix were modeled as elastic isotropic materials. The material properties of the different constituents are provided in Table 2.

### 3 | RESULTS AND DISCUSSIONS

#### 3.1 | Monotonic tensile test results

At the beginning of the experimental approach, tensile tests for various GSM values of WRM and CSM composites were conducted to gain a preliminary understanding of the tensile behavior of these composites. The monotonic quasi-static tensile properties of composites made with various GSM values of WRM and CSM are summarized in Table 3. In the case of the WRM composites, the highest static properties were observed for the 610 gsm variant, followed by 1000 gsm and 800 gsm. The significant difference in the static behavior of the WRM composite can be attributed to the variations in geometrical features. It is important to note that all WRM composites examined in this study featured a plain weave architecture. However, after conducting a detailed characterization of the architecture, significant variations in the bundle dimensions across different WRM composites were identified. Specifically, WRM samples with a fiber mat value of 610 gsm exhibited a lower  $h/a$  ratio, whereas those with 800 and 1000 gsm presented higher  $h/a$  ratios (Table 4). When comparing their respective static properties, it was observed that as the  $h/a$

ratio increases, the static properties decrease, exhibiting the significant effect of the  $h/a$  ratio. Similar evidence can be found in Ref. [37] Among the 800 gsm and 1000 gsm variants, the one with a higher  $g_w/a_w$  ratio exhibited the least static properties. It can also be noticed from Table 3 that WRM composites exhibit the highest tensile strength and tensile stiffness, while CSM composites exhibit the lowest tensile strength and tensile stiffness properties.

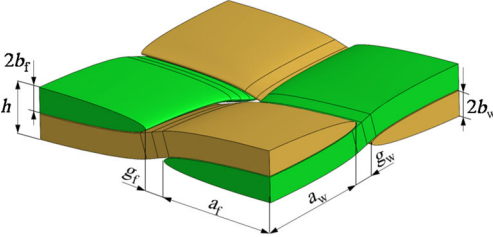
The corresponding tensile stress–strain curves of WRM and CSM glass fiber composites with various GSM values under monotonic tensile loading at room temperature are presented in Figure 4. Overall, the tensile test results indicate that the WRM composites exhibit higher tensile properties compared to CSM composites. This outcome was anticipated due to the higher fiber volume fraction in WRM composites as compared to that in CSM composites. It is also well established that the randomly oriented fibers in CSM lead to a less efficient load distribution along the direction of the applied force. In addition to this, the chopped lengths of the fiber in CSM introduce discontinuities in the resin matrix, leading to the early initiation of micro-cracks at the fiber ends. In contrast, the structure of WRM, which consists of continuous woven glass fibers, ensures that a greater proportion of the fibers contribute to resisting the applied force. Nevertheless, the results obtained from the tensile tests were utilized as a preliminary step to select the appropriate load factors for the fatigue tests of WRM (1000 gsm) and CSM (450 gsm).

Images of typical fracture surfaces (along front and edge views) of WRM (1000 gsm) and CSM (450 gsm) specimens under monotonic tensile loading are presented in Figure 5A. The fracture samples under monotonic loading, when observed from the front view, exhibit a very jagged structure for WRM. Moreover, when observed from the edge, the woven nature of the fiber tends to protrude outwards following tensile failure. In contrast, the CSM composite failed in a brittle manner, with the fracture spanning across the width of the sample. However, both WRM and CSM composites demonstrated that the tensile failures

**TABLE 3** Monotonic quasi-static tensile properties of various GSM values of WRM and CSM composites.

Material	Property	Average (MPa)	Standard deviation (MPa)	Coefficient of variance (%)
WRM (610 gsm)	Tensile modulus, $E$	24891.6	1067.4	4.3
	ultimate tensile strength, $\sigma_{UTS}$	421.2	13.7	3.3
WRM (800 gsm)	Tensile modulus, $E$	19002.3	1348.3	7.1
	ultimate tensile strength, $\sigma_{UTS}$	282.4	13.7	4.9
WRM (1000 gsm)	Tensile modulus, $E$	21,727	539.1	2.4
	ultimate tensile strength, $\sigma_{UTS}$	308.5	12.9	4.2
CSM (300 gsm)	Tensile modulus, $E$	12,099	1147.7	9.5
	ultimate tensile strength, $\sigma_{UTS}$	146.2	7	4.8
CSM (450 gsm)	Tensile modulus, $E$	10,634	869.7	8.2
	ultimate tensile strength, $\sigma_{UTS}$	140.4	3.1	2.2

**TABLE 4** Geometrical features of various GSM values of WRM composites. Units are in mm.

Woven fabric nomenclature	Geometrical feature	WRM (610 gsm)	WRM (800 gsm)	WRM (1000 gsm)
	Major axis of the ellipse, weft bundles ( $2a_f$ )	$3.721 \pm 4.7\%$	$4.831 \pm 10.1\%$	$4.942 \pm 3.3\%$
	Minor axis of the ellipse, weft bundles ( $2b_f$ )	$0.288 \pm 3.9\%$	$0.492 \pm 12.5\%$	$0.485 \pm 6.5\%$
	Gap between adjacent weft bundles ( $g_f$ )	$0.479 \pm 31.8\%$	0	$0.062 \pm 83.6\%$
	Major axis of the ellipse, warp bundles ( $2a_w$ )	$4.007 \pm 3.4\%$	$4.639 \pm 5.2\%$	$4.531 \pm 2.1\%$
	Minor axis of the ellipse, warp bundles ( $2b_w$ )	$0.249 \pm 2.9\%$	$0.507 \pm 4.5\%$	$0.620 \pm 2.5\%$
	Gap between adjacent warp bundles ( $g_w$ )	$0.065 \pm 23.2\%$	$0.792 \pm 18.4\%$	$0.400 \pm 28.6\%$
	Thickness of the fabric layer ( $h$ )	$0.46 \pm 7.1\%$	$0.803 \pm 11.3\%$	$0.876 \pm 15.6\%$
	$h/a_w$	0.22	0.34	0.38
	$g_w/a_w$	0.03	0.34	0.17

occurred away from the gripping area. The location of the fracture surface further confirms that failure was not due to stress concentration effects at the grip section. This evidence strongly suggests that the failure was not structurally driven but rather due to material properties.

### 3.2 | Fatigue test results

Fatigue testing of WRM (1000 gsm) and CSM (450 gsm) composites was conducted at different load factors to obtain the SN curve. The fatigue SN curve was plotted

with the number of cycles to failure ( $N_f$ ) on the X-axis using a semi-log scale and the maximum stress ( $\sigma_{max}$ ) on the Y axis. SN curves to crack initiation and failure obtained from fatigue tests for WRM (1000 gsm) and CSM (450 gsm) are shown in Figure 6A. It is observed that the CSM composite exhibits inferior fatigue resistance, while the WRM composite shows better fatigue resistance.

Both the composites were made to run up to 100,000 cycles, in accordance with the Ref. [26]. This was done with the objective of inducing sufficient damage to enable a fair and unbiased comparison of the material's

performance under fatigue. In the case of the WRM composite, data from the “run out” test, where WRM specimens endured the specified number of cycles without experiencing any failures, were included in the SN curve. This is represented by a horizontal arrow indicating the progression of cycle numbers. For the WRM composite, “run out” test data were crucial for selecting the

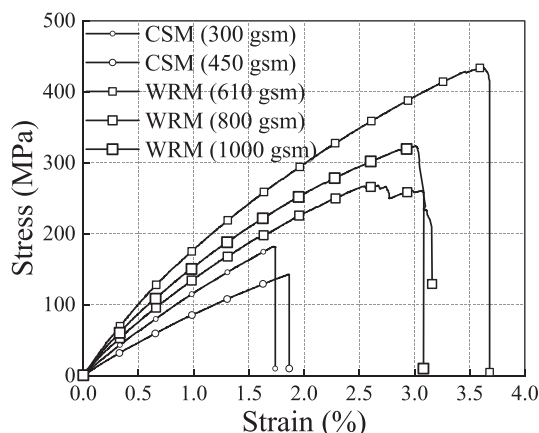


**FIGURE 4** Tensile stress–strain curves of CSM and WRM glass fiber composite under monotonic tensile loading at room temperature.

maximum stress level for interrupted fatigue testing. The corresponding load factor was employed for the CSM composite as well.

The damage in these composites depends on the fiber orientation and weaving pattern for a given number of load cycles. Figure 6B illustrates the variation in normalized modulus degradation with respect to the number of cycles ( $N$ ) for both WRM (1000 gsm) and CSM (450 gsm) composites. Throughout the plot, it is observed that degradation in the modulus is lower in the CSM (450 gsm) composite compared to that in the WRM (1000 gsm). This difference can be attributed to the inherent structural differences and their respective responses to external loads. In the WRM composite, the weaving phenomenon leads to efficient load transfer along the fiber direction. However, this weaving phenomenon makes the composite more susceptible to degradation in the stiffness occurring due to the fibers that are perpendicular to the loading direction. The WRM composites are prone to meta-delamination, which can propagate more easily within the organized fiber structure, leading to a quicker reduction in stiffness. On the other hand, the randomly oriented fibers in the CSM composite can mitigate the damages commonly observed in the WRM composite. The absence of preferential pathways for crack propagation can slow down the degradation of modulus over time.

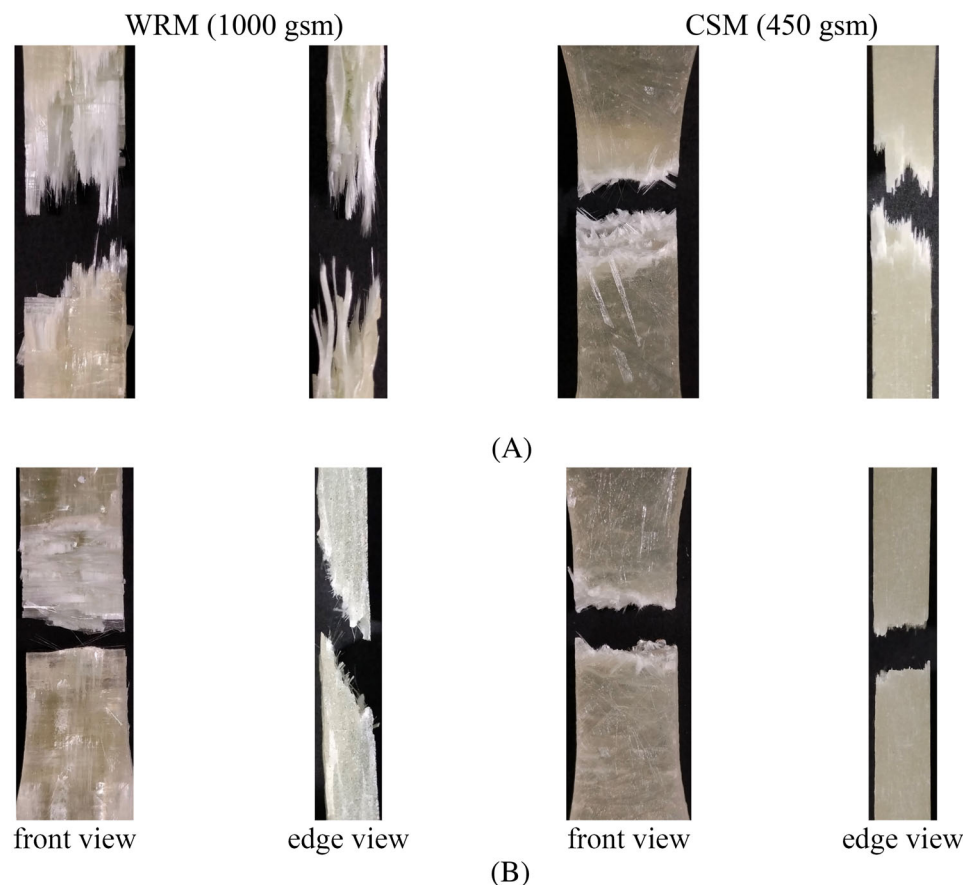


**FIGURE 5** The typical fracture surface of WRM (1000 gsm) and CSM (450 gsm) glass fiber composite under (A) monotonic tensile and (B) tension-tension cyclic loading conducted till failure.



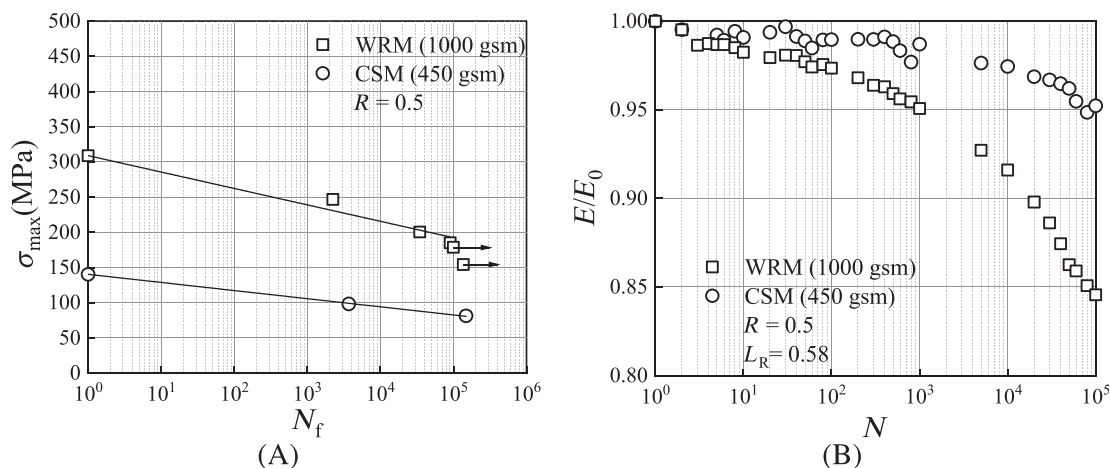


**FIGURE 6** (A) Fatigue S-N curves and (B) normalized modulus degradation of WRM (1000 gsm) and CSM (450 gsm) at  $R = 0.5$  (semi-log scale).

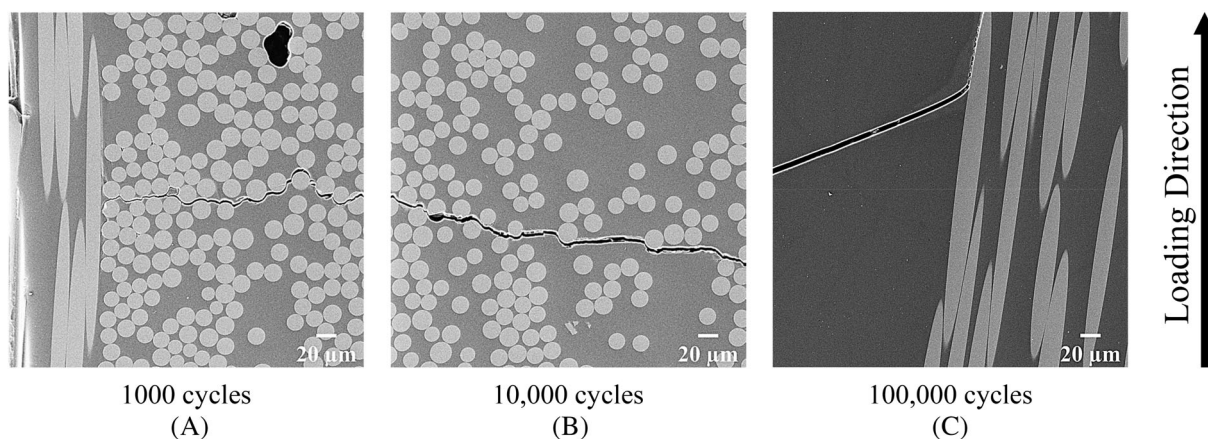


**FIGURE 7** SEM micrographs of WRM (1000 gsm) illustrating damage mechanism for  $R = 0.5$  observed on the edge view. (A) At 1000 cycles, the development of interface cracks only along perpendicular to the loading direction. (B) At 10,000 cycles, propagation of interface crack only along perpendicular to the loading direction. (C) At 100,000 cycles, deviation of matrix crack along the fiber direction leads to meta-delamination. The images were taken using the SE detector.

Images of typical fracture surfaces of WRM (1000 gsm) and CSM (450) specimens under cyclic loading are presented Figure 5B. However, under cyclic loading, the fractured surface of the WRM composite appears less jagged and is perpendicular to the direction of loading. A similar, although less pronounced, effect is observed for the CSM composite.

### 3.3 | Microstructural damage behavior

#### 3.3.1 | Qualitative damage analysis

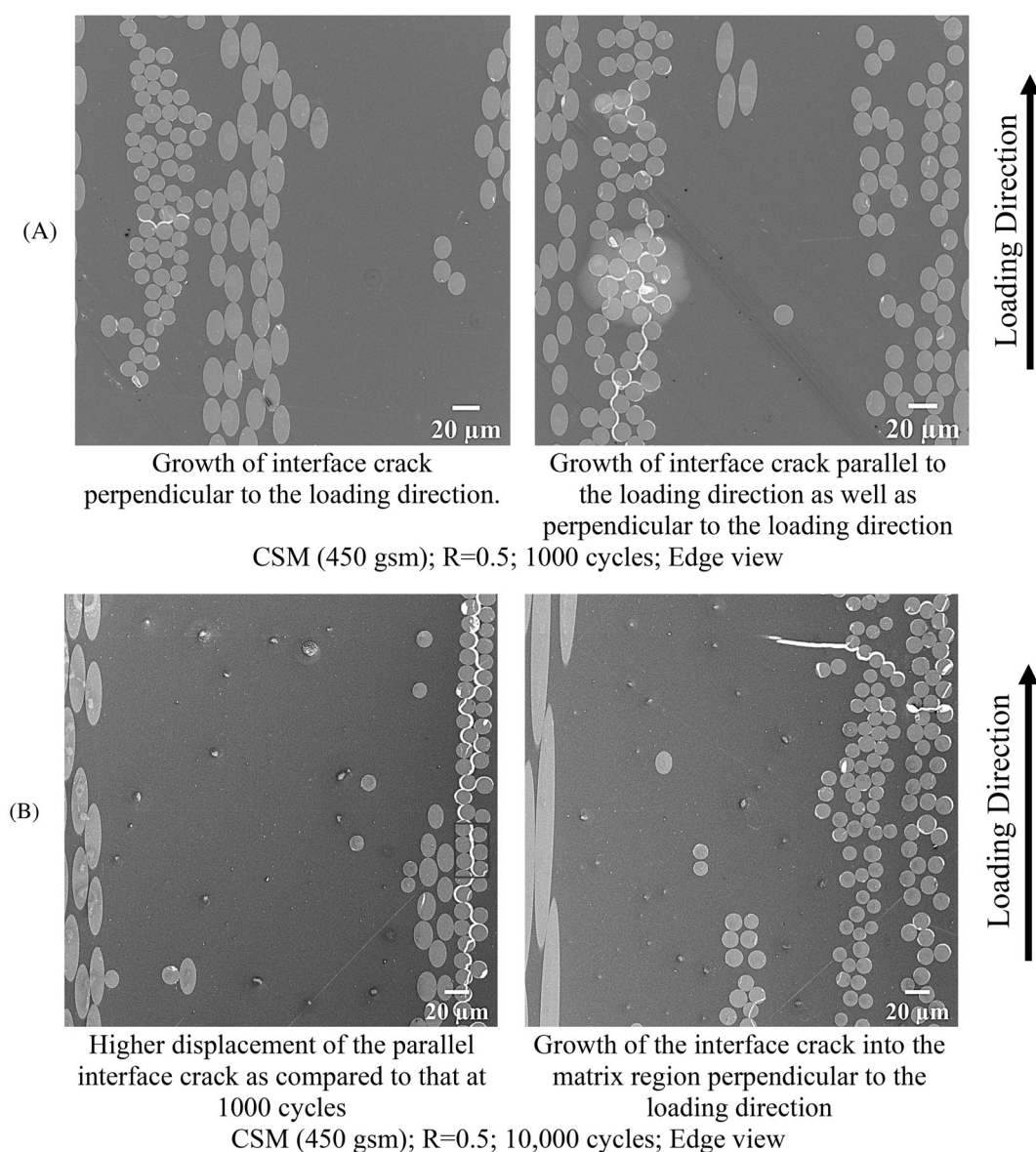
In this section, a qualitative examination of the damage development is carried out at the micro-scale by observing the specimen's edge micrographs.

Figure 7A–C illustrates the damage mechanisms occurring at  $R = 0.5$  in the WRM composite. From the edge observations, the fatigue cracks appear to be perpendicular to the applied loading direction at 1000 cycles. At 10,000 cycles, there is propagation of these interface crack perpendicular to the loading direction. At 100,000 cycles, the matrix cracks deviate along the fiber direction leading to meta-delamination. The cause of this is well documented in several research studies.

A different damage mechanism instead was observed for the CSM composite. CSM is characterized by randomly oriented fibers, yet within this randomness, fibers are clustered, with each cluster having fibers oriented in the same direction. However, each fiber cluster itself is randomly oriented. Another unique aspect of this composite is its low volume fraction of glass fiber. Under

tension-tension fatigue loading, cracks typically initiate at the interface between fiber and matrix, perpendicular to the loading direction. Now, since fibers are oriented in all possible orientations, only a small fraction of them are oriented perpendicular to the loading direction, details of which are discussed in the quantitative microscopy section. Consequently, these fibers are the most likely to experience interfacial cracking (Figure 8A). It is observed that any fiber which has an elliptical shape does not have an interface cracked. Because fibers are bunched in clusters with the same orientation, fiber-matrix debonding tends to concentrate in clusters perpendicular to the loading direction. The high density of interfacial cracking leads to stress concentrators which start triggering cracks

parallel to the loading direction. Interestingly, these parallel cracks predominantly appear in the central regions of the specimen's thickness rather than at the edges, aligning with observations noted in figure 13 of Ref. [28]. Figure 2 displays an example of the location of a parallel crack, and its enlarged view is depicted in Figure 8A. The authors suggest that the low fiber volume fraction, as listed in Table 1, plays a crucial role in this phenomenon. Under tension-tension fatigue, areas with a high density of fibers exhibit less deformation strain. Thus, if a low-volume fraction region is adjacent to a high-volume fraction region with fibers perpendicular to the loading direction, differential strains between the fiber-rich and matrix-rich areas occur. This differential strain is believed



**FIGURE 8** SEM micrographs of CSM (450 gsm) explaining the damage evolution for  $R = 0.5$  at (A) 1000 cycles and (B) 10,000 cycles observed on the edge view. The images were taken using the in-lens detector.

to generate shearing stress, a subject elaborated upon in the numerical analysis section. With pre-existing cracks at the fiber interfaces, shear stress promotes cracking of the fiber-matrix interface parallel to the loading direction. It is clearly observed that this always happens when fiber clusters that are perpendicular to the loading direction are in the vicinity of a resin-rich region (Figure 8B). Eventually, the fiber-matrix interface crack extends into the matrix as well. For a matrix region that is bound between fibers that are not perpendicular to the loading direction as in Figure 9 (being not perpendicular to the loading direction these fibers do not have interfacial cracking), the matrix starts forming a crack by itself.

In WRM also, the initial crack starts at the fiber-matrix interface for fibers perpendicular to the loading

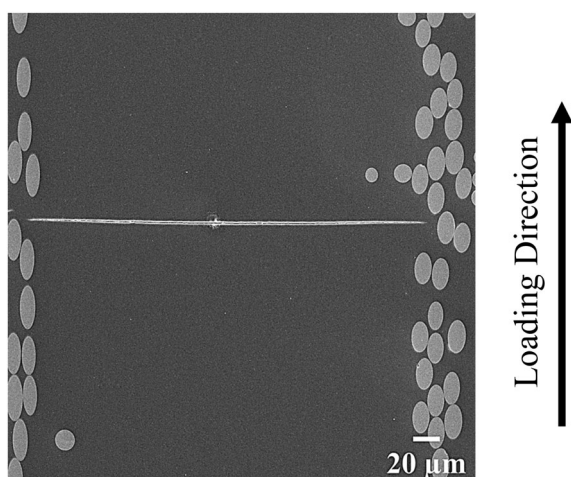


**FIGURE 9** SEM micrographs of CSM (450 gsm) explaining the damage evolution for  $R = 0.5$  at 100,000 cycles observed on the edge view; Propagation of matrix crack perpendicular to the loading direction. The images were taken using the SE detector.

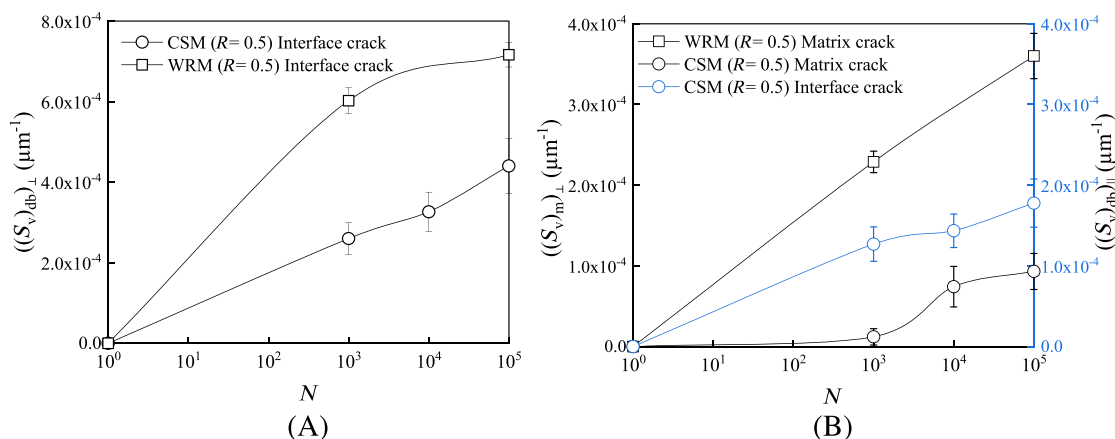


**FIGURE 10** Quantification of true microstructural damage. (A) Perpendicular interface debonding surface area per unit volume and (B) Perpendicular matrix crack surface area per unit volume and parallel interface debonding surface area per unit volume on a plane perpendicular to the loading direction with number of cycles for WRM (1000 gsm) and CSM (450 gsm) specimen at  $R = 0.5$ .

direction. However, the weaving pattern prevents the development of shear stress in the loading direction, thereby inhibiting crack formation parallel to the loading direction. Additionally, the glass fiber volume fraction in WRM composites significantly exceeds that of CSM composites, resulting in fewer large resin-rich areas. Therefore, the mechanisms of damage initiation and propagation differ significantly between the two materials. Despite being subjected to tension-tension fatigue, it is observed that cracks propagate parallel to the loading direction in CSM, but it is never observed in WRM.

### 3.3.2 | Quantitative damage analysis

In this section, the damage progression with respect to a number of cycles in CSM and WRM composites is quantified using SEM and stereology techniques. At least 45 micrographs were observed for damage quantification using a stereological sampling technique for each fatigued sample.

The variation in perpendicular interface debonding surface area per unit volume  $((S_v)_{db})_{\perp}$ , perpendicular matrix crack surface area per unit volume  $((S_v)_{m})_{\perp}$ , and parallel interface debonding surface area per unit volume  $((S_v)_{db})_{\parallel}$  on a plane perpendicular to the loading direction with number of cycles ( $N$ ) for WRM (1000 gsm) and CSM (450 gsm) specimens is presented in Figure 10. From Figure 10A,B, it is evident that perpendicular interface debonding and matrix cracking are more pronounced in WRM composites than in CSM composites. This is because, as it will be discussed in the next section, in CSM composites only a small fraction of fibers are oriented transverse to the loading direction as compared to WRM composites. Consequently, the load transfer to transverse



fibers leads to higher perpendicular interface debonding in WRM composites and subsequent perpendicular matrix cracking. However, the quantitative data in Figure 10B illustrates that parallel interface debonding is higher at all numbers of cycles compared to perpendicular matrix cracking in CSM composites. This indicates that the local clustering of the fibers in CSM composites has a substantial influence on parallel interface cracking than on matrix cracking. These findings elucidate the importance of parallel interface cracking in CSM composites.

It is crucial to recognize that properties are a direct function of microstructural damage state. The aforementioned quantitative data reflect the true microstructural damage within the examined materials, serving a key purpose. It enables the establishment of a direct correlation between microstructural damage states and the degradation of mechanical properties,<sup>26,38</sup> which is essential for developing predictive models capable of estimating the lifespan and performance of these composite materials.

## 4 | DISCUSSION

According to micro-scale analyses presented in Section 3.3, Figures 7 and 8 clearly demonstrate that under tension-tension cyclic loading, perpendicular cracks initiated and propagated in both composites. Moreover, cracks parallel to the loading direction were also observed in the CSM composite, significantly contributing to the damage development process. Hence,

from the experimental observations, the damage state and failure pattern in the CSM composites differed from those in the WRM composites. Considering these new findings, future studies could utilize them as mechanistic basis for developing the necessary analytical expressions for fatigue modelling of parallel cracks. In the following, image analysis was carried out to understand the orientation distribution of the fibers.

Micrographs taken at higher magnification (1000×) were utilized to measure the orientation distribution of the fibers in the CSM composite. Initially, the micrographs were segmented using simple thresholding in image processing software (Fiji ImageJ).<sup>39</sup> However, this resulted in binary images where fibers appeared to be touching each other, which was not the case in reality. To separate the apparently touching fibers, the watershed algorithm in Fiji was employed. The watershed image was then used to measure the ellipse's major and minor axes with the help of the Analyze tool in ImageJ.<sup>40</sup> The quantitative plot of the observed orientation of the fibers is shown in Figure 11B, which provides the fiber orientation distribution in the CSM composite measured using the ellipse major-minor axis method. It can be noticed that the fibers in the CSM composites are oriented in all possible orientations. However, only a small fraction of them have a zero-degree orientation. It is important to note that in this plot, fibers with an orientation perpendicular to the loading direction are denoted as having a zero-degree orientation. Consequently, these fibers become the most probable to have their interface form a crack.

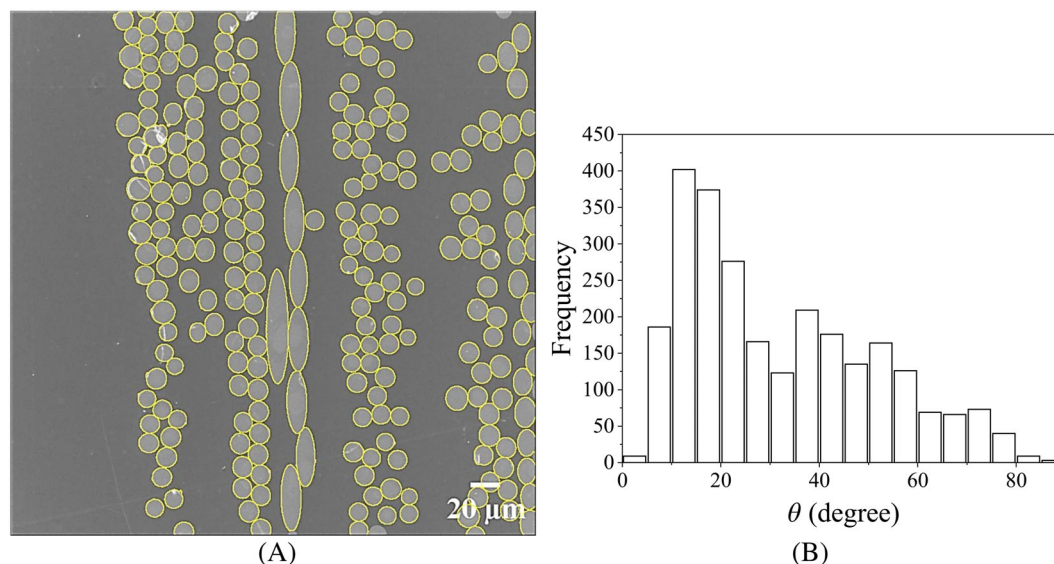


**FIGURE 11** (A) Example of fiber detection in a CSM (450 gsm) composite using Watershed algorithm. (B) Fiber orientation distribution in CSM composite measured using ellipse major-minor axis. Note that the circular fibers are the ones that are perpendicular to the loading direction and are represented with zero degrees of fiber orientation. The frequency data is generated by montages of high-resolution SEM images.



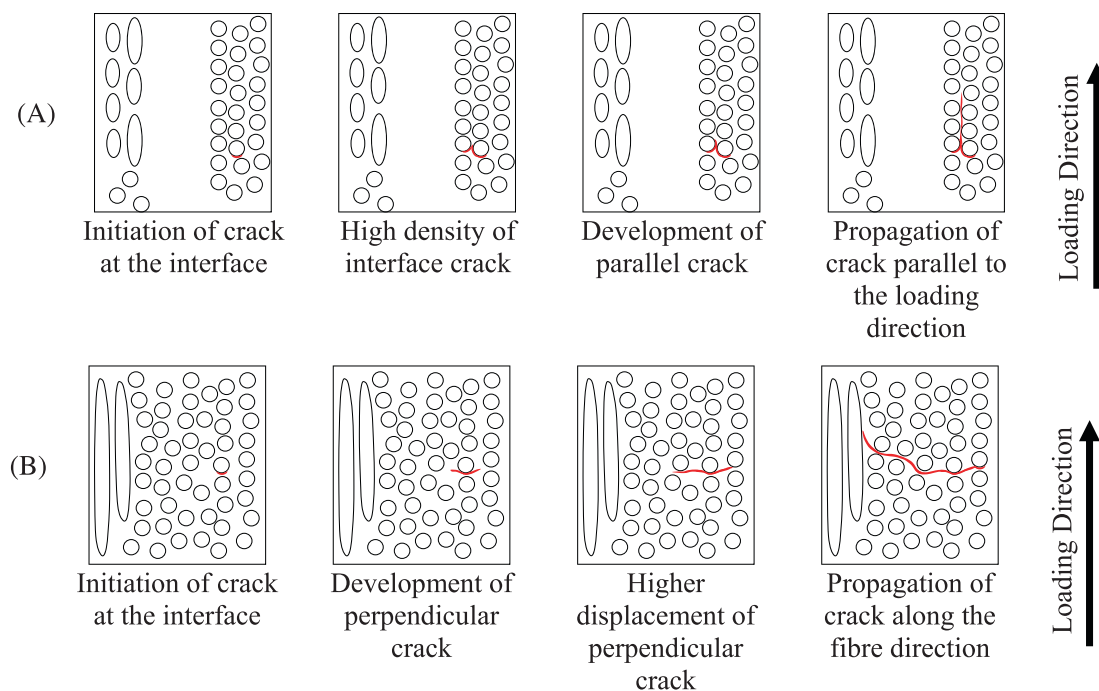


**FIGURE 12** Schematic of the mechanism of crack initiation location and propagation in (A) CSM composite and (B) WRM composite under tension-tension cyclic loading.

#### 4.1 | Numerical analysis

Concerning the difference between the damage mechanisms, it has been rigorously proved in several literatures that in the case of WRM composite, interface cracks initiate within the bundles oriented perpendicular to the loading direction.<sup>13,41</sup> Subsequently, the sequence of damage development follows such that these perpendicular cracks propagate along the entire bundle thickness and then deviate along the fiber direction, leading to meta-delamination (see the schematic in Figure 12B).

Conversely, in the case of CSM composite, the fibers are oriented in all possible directions, with some fibers clustered together as well. Within these clusters, all fibers are oriented in one direction. However, only a small fraction of them are oriented perpendicular to the loading direction, as described earlier (Figure 11). Under tension-tension fatigue loading, perpendicular fibers are the most probable fibers to have their interface form a crack. Since fibers are bunched in clusters with the same orientation, fiber-matrix debonding also becomes concentrated in these clusters, which are perpendicular to the loading direction. This high density of interfacial cracking leads to the formation of stress concentrators, which begin to trigger cracks parallel to the loading direction (see the schematic in Figure 12A). To substantiate this, a section of the microscopic image containing six fibers was chosen for FE simulation, as depicted in Figure 13A. The RVE dimensions

were set to  $97.06 \times 97.06 \times 97.06 \mu\text{m}$ .<sup>3</sup> The fiber diameter was chosen to be  $20 \mu\text{m}$ , and the fiber volume fraction was equal to 0.20, as measured for CSM (450 gsm). The model was meshed with 3D hexahedral elements (C3D8R) and a global element size of  $2 \mu\text{m}$  was adopted according to a mesh sensitivity analysis. A transverse tensile load corresponding to 81 MPa was applied as it corresponds to the load ratio of 0.58 of tensile strength used in the fatigue experiment. Prior to applying load, multipoint constraints were applied on all six faces, ensuring that the displacement of all points on a particular face is the same in that respective direction.<sup>42</sup> This precaution ensures that the faces remain flat. As observed from the simulation (Figure 13B), regions with high fiber density exhibit lower deformation strain. Furthermore, the loading creates differential strains in the fiber and the matrix-rich region. Hence, this differential strain leads to the development of shear stress between the fiber and the matrix-rich region, as seen in Figure 13C.

A final intriguing consideration can be made on the potential of the new findings for advancing the development of fatigue-resistant non-structural GFRPs. As quantitatively demonstrated for the CSM composite in Figure 11 and observed for the WRM composite in Figure 7, fibers oriented perpendicular to the loading direction are the most likely to have their interface form a crack. Therefore, a microscale study of damage mechanisms provides clear insight into the weaker microstructural elements. Based on this understanding, the damage resistance of these composites can be enhanced by tailoring the microstructure of the

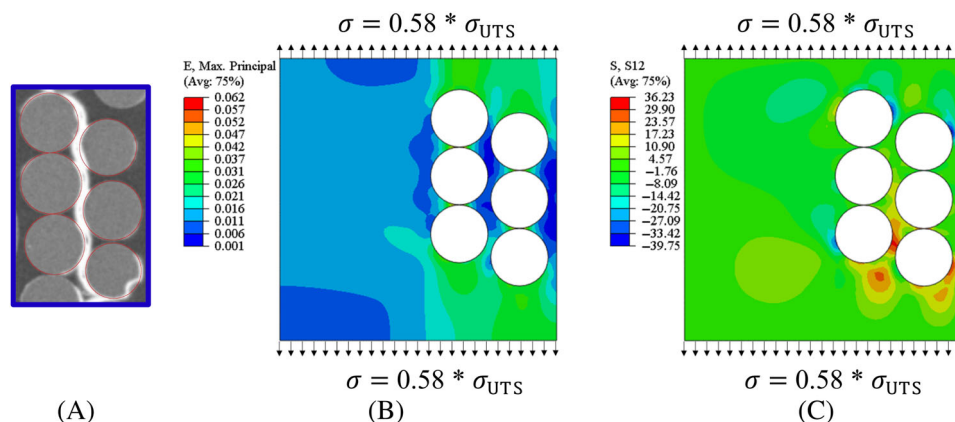


**FIGURE 13** Detailed FE analysis of CSM to demonstrate the existence of differential strains in the fiber and matrix-rich region, and shear stress due to the differential strain. (A) A section of the original grayscale SEM micrograph (Figure 8B) of CSM (450 gsm) composite having fatigue cracks parallel to the direction of loading taken as RVE for numerical analysis. (B) Strain distribution and (C) Shear stress distribution in matrix observed in CSM composite.

material, which involves controlling the spatial distribution and orientation of fibers to optimize mechanical properties. In terms of spatial arrangement, techniques such as varying the volume fraction and distribution of fibers in different regions of the composite could be used to reinforce areas that are subject to higher stresses. For instance, as reported in Ref. [43], gradient microstructures demonstrate significantly higher damage resistance compared to clustered microstructures, as observed in the CSM composite (Figure 8B). Regarding the orientation of fibers, observations from the CSM composite (Figures 8 and 9) indicate that fibers perpendicular to the loading direction were prone to interface cracking. To mitigate this issue, these fibers can be strategically aligned at certain angles relative to the loading direction, thereby reducing stress concentrations. Moreover, reducing the diameter of the fibers can also help decrease stress concentrations by increasing the interface area between the fibers and the matrix for a given volume fraction. This larger interface area enhances the stress transfer capabilities between the fiber and the matrix, potentially reducing the likelihood of stress concentrations and enhancing damage resistance.<sup>44</sup> Moreover, as reported in a previous study,<sup>45</sup> controlling the spatial distribution of the fibers, along with the use of carbon nanotubes, could further minimize local high-stress concentrations due to small inter-fiber distances.

## 5 | CONCLUSION

In this work, microstructural damage in CSM and WRM composites was investigated under tension-tension cyclic loading to improve the understanding of the initial fatigue damage mechanisms. Commencing with the static tensile

tests provided an initial insight into the tensile characteristics of both WRM and CSM composites. It was observed that WRM composites demonstrated superior tensile properties in comparison to their CSM counterparts. These findings, regardless of the circumstances, served as a foundational basis for advancing into the subsequent fatigue testing phase. Fatigue damage mechanisms in these composites were then examined using advanced imaging techniques, consisting of SEM imaging of edge sectional planes. This analysis revealed that, in addition to perpendicular cracks, fatigue cracks parallel to the loading direction were observed in CSM composites, but not in WRM composites. In CSM, perpendicular cracks were observed only on fibers perpendicular to the loading direction. These cracks at the fiber-matrix interface later extended to the perpendicular cracks in the matrix, particularly in CSM composites with a low volume fraction of fibers. In the absence of perpendicular fibers in CSM, cracks are initiated perpendicular to the loading direction within the matrix itself. Finite Element analysis showed that the formation of cracks parallel to the loading direction was due to shear stress, corroborating the observed phenomenon of parallel crack development in CSM composites. The significance of these observed damages was also quantitatively measured, revealing that microstructural damages (interface debonding and matrix crack) increase nonlinearly with the number of cycles. Furthermore, the local clustering of the fibers in CSM composites strongly influenced the interface cracking compared to matrix cracking.

Although this study primarily focused on the initial stages of crack formation, its implications extend far beyond this initial phase. The new findings from this research provide crucial knowledge on the fundamental importance of the identification of preferred locations for

crack initiation. By leveraging insights from the initial crack development processes, along with knowledge of the stress-life curve of CSM composites and suitable cumulative fatigue damage rules, one can delve deeper into understanding the mechanism of fatigue crack propagation. Moreover, this investigation could serve as foundational information for examining behavior under compression-compression and tension-compression loading conditions. Given its scope, these refinements are reserved for future studies.

## ACKNOWLEDGMENTS

The authors would like to deeply acknowledge the support provided by Carl Zeiss Microscopy GmbH in obtaining the high-resolution SEM images. The generous technical assistance provided by Aalen University is greatly appreciated. Acknowledgment is also due to Sunrise Industries (India) Ltd., who provided all the GFRP materials required to carry out the experimental work. The authors wish to thank the Advanced Mechanical Testing Facility (AMTF) for providing the equipment support for tensile and fatigue testing. The authors would like to acknowledge IGSTC-Ph.D. Industrial Exposure Fellowship (PIEF) awarded by the Indo-German Science and Technology Centre for this research collaboration and travel to Germany.

## DATA AVAILABILITY STATEMENT

Data sharing is not applicable to this article as no new data were created or analyzed in this study.

## ORCID

Asim Tewari  <https://orcid.org/0000-0003-2563-060X>

## REFERENCES

- Rajendran S, Arkadu JP, Dinakaran SV, Ganapathy D, Ramana Murthy MV. Application of GFRP for unbundled submarine pipeline in shallow water of Coral Islands. *J Pipeline Syst Eng Pract.* 2018;9(4):04018023-1-04018023-13. doi:10.1061/(asce)ps.1949-1204.0000343
- Rawles JD, Roscow JA, Phillips MG. Effect of transient overloads on the long term performance of glass fibre reinforced polymer (GFRP) pipes for power station cooling water systems. *American Society of Mechanical Engineers, Pressure Vessels and Piping Division (Publication) PVP.* Vol 196; 1990:17-21.
- Owen M. Static and fatigue strength of glass chopped strand mat/polyester resin laminates. In: Sanders B, ed. *Short Fiber Reinf Compos Mater.* ASTM International; 1982:64-84. doi:10.1520/STP29379S
- Sun X, Cui H, Bao Z, Huang L, Huang S, Han W. Fatigue behavior and modeling of chopped carbon fiber reinforced sheet molding compound composites. *Polym Compos.* 2022; 43(5):3150-3166. doi:10.1002/PC.26607
- Tang H, Zhou G, Chen Z, et al. Fatigue behavior analysis and multi-scale modelling of chopped carbon fiber chip-reinforced composites under tension-tension loading condition. *Compos Struct.* 2019;215:85-97. doi:10.1016/j.compstruct.2019.02.041
- Zhang L, Liu Z, Wu D, Zhang H, Zhu P. Fast and synergetic fatigue life prediction of short fiber reinforced polymer composites from monotonic and cyclic loading behavior. *Compos Sci Technol.* 2023;241:110121. doi:10.1016/j.compscitech.2023.110121
- Sul JH, Prusty BG, Pan JW. A fatigue life prediction model for chopped strand mat GRP at elevated temperatures. *Fatigue Fract Eng Mater Struct.* 2010;33(8):513-521. doi:10.1111/J.1460-2695.2010.01460.X
- Shokrieh MM, Esmkhani M, Taheri-Behrooz F. Fatigue modeling of chopped strand mat/epoxy composites. *Struct Eng Mech.* 2014;50(2):231-240. doi:10.12989/sem.2014.50.2.231
- Ye L. On fatigue damage accumulation and material degradation in composite materials. *Compos Sci Technol.* 1989;36(4): 339-350. doi:10.1016/0266-3538(89)90046-8
- Naik NK. Woven-fibre thermoset composites. *Fatigue in Composites.* Elsevier; 2003:296-313. doi:10.1533/9781855738577.3.296
- Kumar R, Talreja R. Fatigue damage evolution in woven fabric composites. *Collection of Technical Papers-AIAA/ASME/ASCE/AHS/ASC Structures, Structural Dynamics and Materials Conference.* Vol 1. AIAA; 2000:1841-1849. doi:10.2514/6.2000-1685
- Montesano J, Fawaz Z, Bougherara H. Non-destructive assessment of the fatigue strength and damage progression of satin woven fiber reinforced polymer matrix composites. *Compos B: Eng.* 2015;71:122-130. doi:10.1016/j.compositesb.2014.11.005
- Lamon F, Maragoni L, Carraro PA, Quaresimin M. Fatigue damage evolution in woven composites with different architectures. *Int J Fatigue.* 2023;167:167. doi:10.1016/j.ijfatigue.2022.107365
- Lamon F, Carraro PA, Maragoni L, Quaresimin M. A multiscale strategy for assessing the micro-scale stress distribution in the matrix of textile composites. *Compos Part A: Appl Sci Manuf.* 2022;159:107026. doi:10.1016/j.compositesa.2022.107026
- Daggumati S, De Baere I, Van Paepegem W, et al. Fatigue and post-fatigue stress-strain analysis of a 5-harness satin weave carbon fibre reinforced composite. *Compos Sci Technol.* 2013; 74:20-27. doi:10.1016/j.compscitech.2012.09.012
- Xu J, Lomov SV, Verpoest I, Daggumati S, Van Paepegem W, Degrieck J. A comparative study of twill weave reinforced composites under tension-tension fatigue loading: experiments and meso-modelling. *Compos Struct.* 2016;135:306-315. doi:10.1016/j.compstruct.2015.09.005
- Lomov SV, Verpoest I, Peeters T, Roose D, Zako M. Nesting in textile laminates: geometrical modelling of the laminate. *Compos Sci Technol.* 2003;63(7):993-1007. doi:10.1016/S0266-3538(02)00318-4
- Shembekar PS, Naik NK. Elastic behavior of woven fabric composites: II—laminar analysis. *J Compos Mater.* 1992;26(15): 2226-2246. doi:10.1177/002199839202601503
- Daggumati S, Voet E, Van Paepegem W, et al. Local strain in a 5-harness satin weave composite under static tension: part I - experimental analysis. *Compos Sci Technol.* 2011;71(8):1171-1179. doi:10.1016/j.compscitech.2011.03.021
- Daggumati S, Van Paepegem W, Degrieck J, et al. Local strain in a 5-harness satin weave composite under static tension: part II - Meso-FE analysis. *Compos Sci Technol.* 2011;71(9):1217-1224. doi:10.1016/j.compscitech.2011.03.020

21. Crowther MF, Wyatt RC, Phillips MG. Creep-fatigue interactions in glass fibre/polyester composites. *Compos Sci Technol*. 1989;36:191-210.
22. Mandell JF. Fatigue behavior of short fiber composite materials. *Compos Mater Ser*. 1991;4(C):231-337. doi:[10.1016/B978-0-444-70507-5.50011-1](https://doi.org/10.1016/B978-0-444-70507-5.50011-1)
23. Sun X, Li Y, Engler-Pinto C, et al. Characterization and modeling of fatigue behavior of chopped glass fiber reinforced sheet molding compound (SMC) composite. *Int J Fatigue*. 2022;156:106647. doi:[10.1016/j.ijfatigue.2021.106647](https://doi.org/10.1016/j.ijfatigue.2021.106647)
24. Belmonte E, De Monte M, Hoffmann CJ, Quaresimin M. Damage initiation and evolution in short fiber reinforced polyamide under fatigue loading: influence of fiber volume fraction. *Compos B: Eng*. 2017;113:331-341. doi:[10.1016/j.compositesb.2017.01.023](https://doi.org/10.1016/j.compositesb.2017.01.023)
25. Owen MJ, Dukes R. Failure of glass-reinforced plastics under single and repeated loading. *J Strain Anal*. 1967;2(4):272-279. doi:[10.1243/03093247V024272](https://doi.org/10.1243/03093247V024272)
26. Senthilnathan K, Hiremath CP, Naik NK, Guha A, Tewari A. Microstructural damage dependent stiffness prediction of unidirectional CFRP composite under cyclic loading. *Compos Part A: Appl Sci Manuf*. 2017;100:118-127. doi:[10.1016/j.compositesa.2017.05.010](https://doi.org/10.1016/j.compositesa.2017.05.010)
27. Quaresimin M, Ricotta M. Fatigue response and damage evolution in 2D textile composites. In: Carvelli V, Lomov SV, eds. *Fatigue Response and Damage Evolution in 2D Textile Composites*. Woodhead Publishing; 2015.
28. Owen MJ, Howes RJ. The accumulation of damage in a glass-reinforced plastic under tensile and fatigue loading. *J Phys D Appl Phys*. 1972;5:5-1649.
29. Baddeley A, Vedel Jensen EB. *Stereology for Statisticians*. 1st ed. Chapman and Hall/CRC; 2004.
30. Russ JC, Dehoff RT. *Practical Stereology*. Vol 2. Springer; 2000.
31. Underwood EE. In: McCall JL, Mueller WM, eds. *Quantitative Stereology*. Springer; 1973.
32. Seraji SM, Razavi Aghjeh MK, Davari M, Salami Hosseini M, Khelgati S. Effect of clay dispersion on the cell structure of LDPE/clay nanocomposite foams. *Polym Compos*. 2011;32(7):1095-1105. doi:[10.1002/PC.21127](https://doi.org/10.1002/PC.21127)
33. Mortazavian S, Fatemi A. Effects of fiber orientation and anisotropy on tensile strength and elastic modulus of short fiber reinforced polymer composites. *Compos B: Eng*. 2015;72:116-129. doi:[10.1016/j.compositesb.2014.11.041](https://doi.org/10.1016/j.compositesb.2014.11.041)
34. Gamstedt EK, Talreja R. Fatigue damage mechanisms in unidirectional carbon-fibre-reinforced plastics. *J Mater Sci*. 1999;34:2535-2546. doi:[10.1023/A:1004684228765](https://doi.org/10.1023/A:1004684228765)
35. Tewari A, Gokhale AM. Efficient estimation of number density in opaque material microstructures: the large-area disector. *J Microsc*. 2000;200(3):277-283. doi:[10.1046/J.1365-2818.2000.00759.X](https://doi.org/10.1046/J.1365-2818.2000.00759.X)
36. Soden P, Hinton MJ, Kaddour AS. Lamina properties, lay-up configurations and loading conditions for a range of fibre-reinforced composite laminates. *Compos Sci Technol*. 1998;58(7):1011-1022. doi:[10.1016/S0266-3538\(98\)00078-5](https://doi.org/10.1016/S0266-3538(98)00078-5)
37. Naik NK, Ganesh VK. Prediction of on-axes elastic properties of plain weave fabric composites. *Compos Sci Technol*. 1992;45(2):135-152. doi:[10.1016/0266-3538\(92\)90036-3](https://doi.org/10.1016/0266-3538(92)90036-3)
38. Hiremath CP, Senthilnathan K, Naik NK, Guha A, Tewari A. Microstructural damage based modeling of thermal conductivity of cyclically loaded CFRP. *Compos Sci Technol*. 2018;154:37-44. doi:[10.1016/j.compscitech.2017.11.011](https://doi.org/10.1016/j.compscitech.2017.11.011)
39. Schindelin J, Arganda-Carreras I, Frise E, et al. Fiji: an open-source platform for biological-image analysis. *Nat Methods*. 2012;9(7):676-682. doi:[10.1038/nmeth.2019](https://doi.org/10.1038/nmeth.2019)
40. Yotte S, Breyse D, Riss J, Ghosh S. Cluster characterisation in a metal matrix composite. *Mater Charact*. 2001;46(2-3):211-219. doi:[10.1016/S1044-5803\(01\)00126-7](https://doi.org/10.1016/S1044-5803(01)00126-7)
41. Paris F, Correa E, Mantić V. Kinking of transversal Interface cracks between fiber and matrix. *J Appl Mech*. 2007;74:703-716. doi:[10.1115/1.2711220](https://doi.org/10.1115/1.2711220)
42. Melro AR, Camanho PP, Andrade Pires FM, Pinho ST. Micromechanical analysis of polymer composites reinforced by unidirectional fibres: part II-micromechanical analyses. *Int J Solids Struct*. 2013;50:1906-1915. doi:[10.1016/j.ijsolstr.2013.02.007](https://doi.org/10.1016/j.ijsolstr.2013.02.007)
43. Mishnaevsky LL. *Computational Mesomechanics of composites: numerical analysis of the effect of microstructures of composites of strength and damage resistance*. Wiley; 2007:300.
44. Kaw AK. *Mechanics of Composite Materials*. CRC Press; 2005. doi:[10.1201/9781420058291](https://doi.org/10.1201/9781420058291)
45. Romanov VS, Lomov SV, Verpoest I, Gorbatiikh L. Modelling evidence of stress concentration mitigation at the micro-scale in polymer composites by the addition of carbon nanotubes. *Carbon*. 2014;82:184-194. doi:[10.1016/j.carbon.2014.10.061](https://doi.org/10.1016/j.carbon.2014.10.061)

**How to cite this article:** Hiremath MM, Bernthaler T, Anger P, Mishra SK, Guha A, Tewari A. Comparison of damage mechanisms in chopped strand mat and woven roving mat composites under cyclic tension. *Polym Compos*. 2024;1-16. doi:[10.1002/pc.28539](https://doi.org/10.1002/pc.28539)